Alloying effects on oxidation mechanisms in polycrystalline Co-Ni base superalloys

F.B.Ismail[a], V.A.Vorontsov[a], T.C.Lindley[a], M.C.Hardy[b], D.Dye[a], B.A.Shollock[c]

[a] *Department of Materials, Royal School of Mines, Imperial College, Prince Consort Road, South Kensington, London SW7 2BP, UK*
[b] *Rolls-Royce plc, ELT-10, PO Box 31, Derby, DE24 8BJ*
[c] *WMG, University of Warwick, Coventry, CV4 7AL*

Abstract

Oxidation mechanisms in polycrystalline Co-Ni-Cr-Al-W-Ta alloys were investigated using $^{16}O/^{18}O$ isotopic tracer analysis in the focused ion-beam secondary ion mass spectrometer (FIB-SIMS). It was found that Al additions favour the formation of a continuous alumina-rich layer, that Cr indirectly improved oxidation resistance and that increasing the Co fraction resulted in poorer oxidation performance. In the alloy containing 15 at.% Cr and 10 at.% Al, the outer scale formed after 200 h oxidation at 800 °C comprised oxides less than 1 μm thick. It is concluded that protective oxide scales can be formed in Co-Ni base superalloys.

Keywords: A. superalloys, B. SIMS, B. STEM, C. oxidation

1. Introduction

Increased turbine entry temperatures (TET) for improved turbine efficiency push Ni-base superalloys to their operational limits. To meet the demands of increased TET, a new generation of Ni-base superalloys are now being produced through powder metallurgy (P/M). In 2006, a new Co-base alloy family was reported with strength similar to Ni-base superaloys [1]. Sato et al. discovered that the Co-Al-W ternary system contains a $L1_2$ γ' phase, identified as Co_3(Al,W). The development of these alloys is motivated by their potential for (i) improved creep behaviour due to reduced γ' coarsening arising from the low diffusivity of W in the matrix, (ii) reduced freezing range and therefore enhanced castability [2] and (iii) potential for higher stacking fault energies than in Ni, and hence improved creep strengths [3–5]. Ta additions have been investigated [1, 6–9], finding that it is effective for stabilisation of the γ' phase, increasing the solvus temperature [10, 11]. Higher temperatures require excellent environmental degradation resistance in oxidising environments to meet the operational service life of the component. Hence, the alloys studied here include 1 at.% Ta.

One of the primary factor that limits the service life of a component for high temperature applicationas is oxidation, which can lead to the loss of load-bearing capacity in a component by the reduction of metallic cross section [12]. Oxidation of Co-Al-W alloys at 800°C typically produces a multi-layered oxide structure, with Co-rich oxide in the outer layer, a mixed oxide of Co-Cr-Al in the middle layer, whilst the inner layer is suggested to be a protective layer of Al_2O_3 [13–18]. The Al is usually depleted at the oxide / alloy interface to form a continuous layer of Al_2O_3 on the surface. The effects of alloying elements on oxidation behaviour have been investigated in [8, 10, 11, 13–15, 18, 19].

In practice, in many applications the oxidation of metals is managed rather than prevented. Protection of the underlying metal is most often accomplished by the formation of a continuous scale over the surface such that it serves as a barrier between the remaining underlying, unoxidized metal and the environment. Long-term protection is generally associated with a scale that slowly grows whilst simultaneously providing protection from further oxygen attack and avoiding significant depletion of the strengthening precipitates [12]. Protective scale formation is more desirable than coating, as it allows for healing of the scale in the case of surface damage.

The formation of protective, dense, near-stoichiometric Al_2O_3 is desirable in the order to slow down the growth rate, controlled by oxygen diffusion. In general, although both Al and Cr additions are known to improve oxidation resistance up to 900°C [10, 11, 17, 20], relatively small variations in composition may result undesirable changes in the base alloy microstructure, altering the mechanical performance [3], while excessive additions of Cr may lead to a decrease in γ' stability [7]. To address this, Ni was added to a Co-Al-W-Cr alloy to stabilise the γ/γ' microstructure while retaining oxidation resistance [11, 17, 21]. Al additions are detrimental to the stability of the underlying γ/γ' microstructure and yet most importantly forms the protective internal Al_2O_3 scale. For instance, it is well known that a lower aluminum content is needed to establish and maintain an Al_2O_3 scale on M-Cr-Al alloys (where M = nickel, cobalt, or iron) than on M-Al alloys. This phenomenon is generally referred to as the third-element effect. Such an effect can be extremely important from an alloy-design viewpoint, as excessive additions of aluminum, for example, tend to depress the melting point and lead to the formation of embrittling phases [12].

Additions of Cr have been found to be beneficial up to 800°C [22]. In isothermal oxidation tests at 800°C and 900°C, Cr was found to promote the protective Al_2O_3 formation due to selective Al-oxidation [23]. According to an initial suggestion by Wagner [24], the third element, e.g. chromium in M-Al alloys, acts as a getter for oxygen in the alloy during the initial stage, lowering the oxygen solubility in the alloy and preventing internal oxidation of the more reactive component, aluminum, producing external Al_2O_3 layers at lower aluminum levels than in binary M-Al alloys. Yan et. al [11] have previously studied the oxidation resistance of Co-Al-W alloys with Cr-additions and multilayer oxide scales were formed. They observed that the oxide scales exhibit a three-layered structure; the external scale consists of outer Al_2CoO_4, a Cr-rich middle layer, and internal Al_2O_3.

The oxidation behaviour of cobalt-base superalloys can be improved by suitable alloying strategies. For this, different alloying elements, such as nickel, aluminium, and chromium, have been added to Co-Al-W ternary alloys in varying amounts to improve the oxidation behaviour. Since the current understanding of the oxide formation mechanism in Co-Al-W alloys is limited, there is a need to focus on the difference in the oxidation sequence with varying alloy content. The present study evaluates the effects of alloying, particularly Ni, Al and Cr, on the oxidation behaviour of Co-Al-W superalloys. The use of oxygen isotopes to study the transport mechanism during high temperature oxide scale growth is crucial to improving the understanding of the oxide scale. Later in this paper, the effect of additions of these elements on the oxidation mechanism of the Co-base superalloys and the changes to the underlying microstructures at temperatures of 800°C as well as long term oxidation (200 h - 5000 h) will be discussed.

2. Experimental methods

2.1. Material preparation

The alloy powder was manufactured by vacuum induction melting and inert gas atomisation by ATI Powder Metals, Pittsburgh, PA, USA. After powder production, the material was consolidated by hot isostatic pressing (HIP) and isothermally forged by ATI Forged Products, Cudahy, WI, USA. After forging, the material was subjected to a heat treatment of 1050 °C for 30 min, above the solvus temperature of 1000 °C. Table 1 summarises the nominal compositions of alloys with varied Ni, Al, and Cr content. Note that the first two alloys have the same Co/Ni ratio whilst the third alloy has 1.3:1 Co/Ni ratio. Hence 1.3Co is utilised in the alloy abbreviation.

2.2. Oxidation Experiments

Oxidation experiments were carried out in an isotopic exchange oxidation rig. In order to examine the mechanism of oxide formation, two-stage experiments were carried out using oxygen-18 ($^{18}O_2$) at a partial pressure of 0.2 atm. The samples were 5 × 5 × 5 mm in size and surface polished to 1 μm finish using diamond suspension. The samples were first exposed to research-grade oxygen (referred to as $^{16}O_2$) at pO_2 = 200 mbar. The exchange furnace was evacuated before introducing the $^{18}O_2$-enriched oxygen also at pO_2 = 200 mbar. The samples were then fast-cooled in air by rolling off the exchange furnace. For each exposure time, the $^{18}O_2$-enriched oxygen was introduced during the last 24 hours to act as a tracer.

Table 1: Nominal compositions of the investigated alloys and utilised abbreviations.

Alloy	Nominal composition in at. %						γ' solvus
Designation	Co	Al	W	Cr	Ta	Ni	(°C)
17Cr-12Al	33.5	12	3	17	1	33.5	990
15Cr-10Al	36	10	3	15	1	35	1000
1.3Co-17Cr-10Al	40	10	3	17	1	29	1010

Long-term isothermal oxidation experiments were conducted at 800 °C in a box furnace under atmospheric conditions. The samples were placed in alumina crucibles and exposed to laboratory air. After exposure, the samples were taken out of the furnace along with the crucibles which would contain any spalled oxide. All of the samples for both isotopic exchange oxidation and long-term isothermal oxidation were weighed before and after exposure to determine their mass change.

2.3. Characterisation

The microstructure and the chemical composition of the samples were examined using a Zeiss Auriga scanning electron microscope (SEM) equipped with an Oxford Instruments EDX detector. The morphologies of the oxide surfaces were characterised using secondary electron mode. A thin platinum strip with dimensions of 25 × 2.5 × 1.5 μm was deposited on the surface of each of the oxidised samples prior to milling. Trenches milled using a focused ion beam (FIB) were viewed in energy selective backscatter (EsB) mode at 36° relative to the sample surface viewing angle. SEM was chosen to capture microstructure at 1.48kV acceleration voltage at a working distance of 5 mm, in order to identify different phases via atomic number contrast. Imaging was performed at 36 ° from the surface as illustrated in Figure 1. All chemical analyses of the samples were performed using EDX in the SEM mode using a 15−20 kV acceleration voltage. To improve experimental accuracy, each spectrum was collected from at least 5 points.

FIB milling for Secondary Ion Mass Spectroscopy (SIMS) was performed using the FEI FIB200-SIMS, equipped with a 30 keV Ga^+ liquid metal ion gun (LMIG) primary ion column. A trench with dimensions of approximately 25 × 15 × 10 μm was milled using a 20 nA primary ion current. Cross-sectioning applied various milling angles, ranging from 45 ° to 60 ° to the surface to produce ramped sections of the external and internal oxides. The trench wall was successfully polished using 2 nA, 600 pA and 120 pA

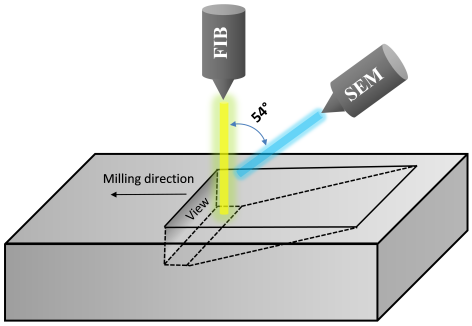

Figure 1: Schematic of a trench FIB milling and viewing of the cross section in SEM mode.

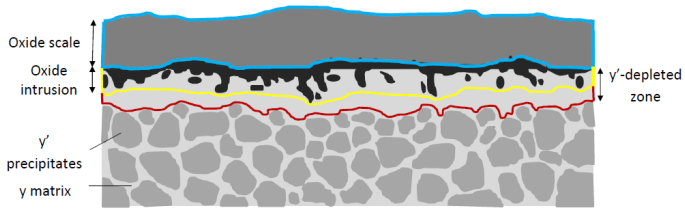

Figure 2: Schematic of a cross section of an oxidised sample highlighting the features commonly observed.

primary ion currents. Imaging was performed using the secondary ion imaging mode at 36 ° - 45 ° to the surface normal using a 30 pA primary ion current.

SIMS was used to obtain high-resolution oxygen ion map in order to elucidate the oxidation behaviour after the oxygen isotope experiments. For the $^{16}O^-$ map, a 300 pA beam was used with a 1 ms dwell time and saved as matrix of 256×221 pixels for further Matlab analysis. For the $^{18}O^-$ map, similar settings were used except the dwell time was 4 ms.

Thin slices of the oxidised specimens were prepared for transmission electron microscopy (TEM). A standard in-situ FIB lift-out technique was used to produce site-specific TEM samples. A Helios Nanolab 600 (FEI) dual-beam apparatus was operated at 30 keV and a platinum gas injection system was used for surface protection. Imaging of the extracted foils was performed using a JEOL JEM 2100F 200 keV field emission gun (FEG) TEM/STEM.

To obtain high resolution lattice images for small grained FIB specimens (thin oxides), an FEI TITAN 80/300 TEM/STEM fitted with a monochromator and an image aberration corrector was used. Frequency domain images (diffraction patterns) were obtained via the Fast Fourier Transform (FFT) using the ImageJ software package. Point EDX analyses were carried out in STEM mode to determine the local chemical compositions in the foils.

2.4. Measurement of surface scale thickness

In the case of thin oxide layers, using the use of conventional metallographic methods of sectioning, hot-mounting, and mechanical grinding were inappropriate due to the fragility of the oxide. Therefore, for thicknesses of each layer in the surface scale cross sections (trenches) (30 × 25 × 15) μm were measured from the FIB trenches using a Zeiss Auriga. Figure 2 shows the schematic of a cross section of the oxidised samples with major oxidation damage characteristics near the surface. The outermost layer which is usually referred to as the surface oxide, is labelled as oxide scale, followed by the oxide alloy interface region, called oxide intrusion and lastly the γ'-depleted zone. The thickness of the damage layers was evaluated as an average value of the thicknesses measured across each area.

3. Results

3.1. Alloy characteristics

The grain structure of as-HIPed, forged and heat-treated samples were examined using electron backscatter diffraction (EBSD). The average grain size in each material condition was calculated from EBSD derived data using the equivalent grain diameter method and disregarding twins boundaries. 1453 grains were detected with average grain size of approximately 2.5 µm, as shown in Figure 3. The grain size distribution was obtained by fitting a Weibull distribution to the cumulative distribution function, giving an average grain size comparable to powder metallurgy Ni superalloys.

The SEM-EsB micrographs in Figure 4 show the FIB cross-section of the base alloys after HIP, forging and heat treatment with γ/γ' grains, sub-µm carbides, the intermetallic (Co-Ni)Al B2 and the topological-closed-packed TCP $(Co\text{-}Ni)_3W$ DO_{19} and $Co_3(W\text{-}Ta)$ phases. Based on previous studies, it is found that these two phases, B2 and DO_{19}, form adjacent to each other and can be recognised by their morphology and atomic number contrast [16, 18, 21, 25]. In the present case, these precipitates were also examined using STEM-EDX in the TEM which, lacking precise crystallography information, is not

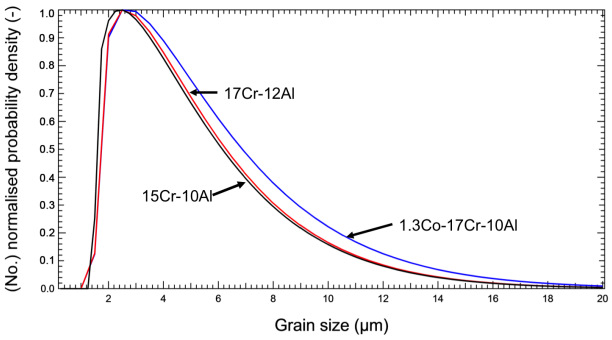

Figure 3: The grain size distributions obtained *via* EBSD using a 0.5 μm step size, 3.6×10^5 points, 1453 grains.

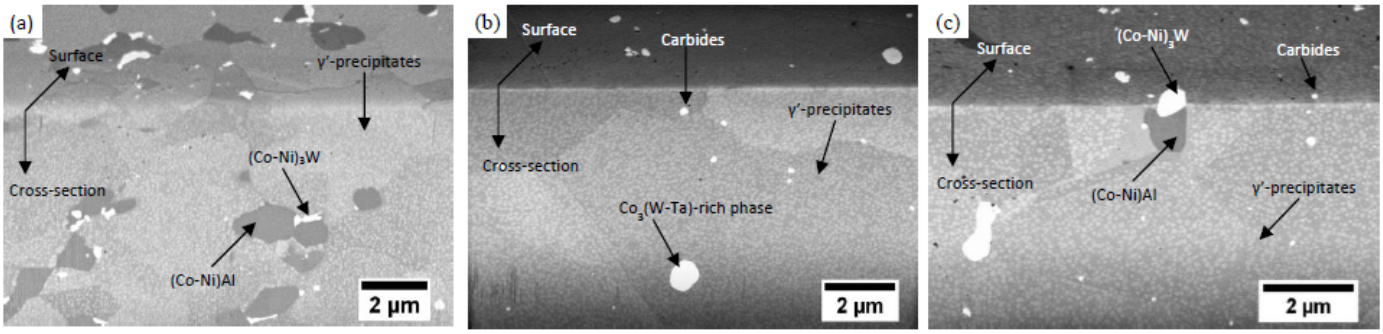

Figure 4: EsB-SEM micrographs of as-HIPed, forged and heat-treated alloy (a) 17Cr-12Al (b) 15Cr-10Al (c) 1.3Co-17Cr-10Al showing the polycrystalline grains with a fine γ/γ' microstructure, carbide precipitates, and secondary phases (B2 and DO_{19}) along the grain boundaries.

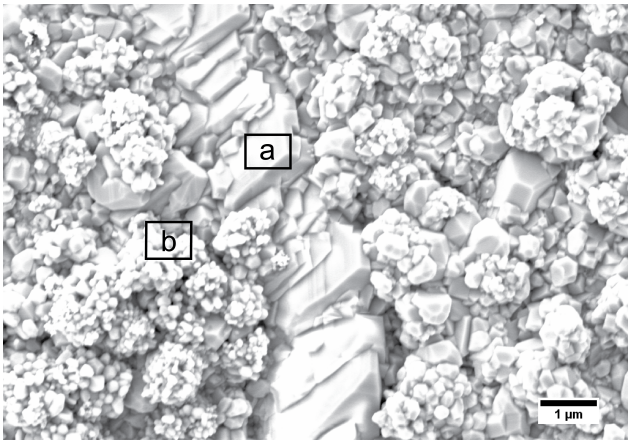

Figure 5: SEM image of two types of oxide scales formed on alloy 15Cr-10Al (a) facetted oxide (b) nodular oxide after 400 h oxidation in laboratory air at 800°C

completely definitive, but does provide enough information to confirm these preliminary phase assignments. The presence of such secondary phases may be detrimental to the mechanical performance and so it is important to understand the effect of Cr and Al additions on the phase equilibria [21]. It is crucial to note that 17% Cr leads to the formation of the B2 phase, as observed in Figure 4(a) and (c).

3.2. Surface oxide morphology

The external scales formed during oxidation for 400 h at 800°C were imaged in the SEM; the morphology of each oxide is distinctive. Figure 5 shows a representative surface oxide structure observed in all three alloys, which features two distinct external scale morphologies. As determined by SEM-EDX analysis, the approximate compositions of the two scales are; a) Al-rich, Al-Co-Ni oxide (approximately 22Al-10(Co+Ni)-68O (at.%)) and b) Cr-rich, (approximately 24Cr-12(Co+Ni)-64O (at.%)). Both possessed a similar Co+Ni content. It can be noted that the facetted aluminium-rich oxide formed preferentially on grain boundaries whilst the nodular Cr-rich oxide formed on the remaining grain surfaces.

3.3. Oxidation after 200 h

Figure 6 shows the SEM-EsB microstructures of oxidised 17Cr-12Al, 15Cr-10Al, 1.3Co-17Cr-10Al after 200 h oxidation at 800°C. Alloy 17Cr-12Al proved to have a very good oxidation resistance, forming a continuous Al_2O_3 layer with a very thin external oxide. The underlying bulk material featured a very fine γ/γ' structure as well as coarse intermetallic phases B2 (Co-Ni)Al and DO_{19} $(Co\text{-}Ni)_3W$.

As we reduce the Cr content from 17% to 15% and Al content from 12% to 10%, good oxidation resistance is still observed, with alloy 15Cr-10Al also forming a continuous Al_2O_3 layer as well as blocky internal oxides. The DO_{19} phase is rich in W and Ta, Co_3(W-Ta). The γ' fraction in the bulk is reduced as most of the Al has diffused out towards the surface to form the protective Al_2O_3 layer. As the proportion of Co is increased to give Co:Ni ratio of 1.3:1, and Cr is increased to 17%, the formation of non-continuous Al_2O_3 layer resulted in an increase in the thickness of the external scale.

3.4. Oxidation after 300 h

After 300 h, thicker oxides were formed on the surface as shown in Figure 7. Major changes can be seen in the scale thickness of Cr_2O_3 and the formation of recrystallised grains in the γ'-depleted zone. Only alloy 17Cr-10Al forms a continuous protective Al_2O_3 scale, though there is a thick external oxide layer on the surface as shown Figure 7(a).

The unique observation in alloy 15Cr-10Al are the recrystallised grains that formed in the γ'-depleted zone (Figure 7 b). The internal oxide (Al_2O_3) was mostly found to form on the surface as well as intergranularly in the region of recrystallised grains. Although the consistency of a thin oxide scale thickness of this alloy is pronounced, compared to the other two alloys, the presence of voids between the external and internal oxides is of concern.

An issue of even greater concern is the spallation of external oxide, which in this case, was observed in alloy 1.3Co-17Cr-10Al. A trench was FIB milled in an area where the oxide had spalled, as seen in Figure 7c. A thin external oxide which is almost completely delaminated can be seen on the surface. Even though there was no trace of

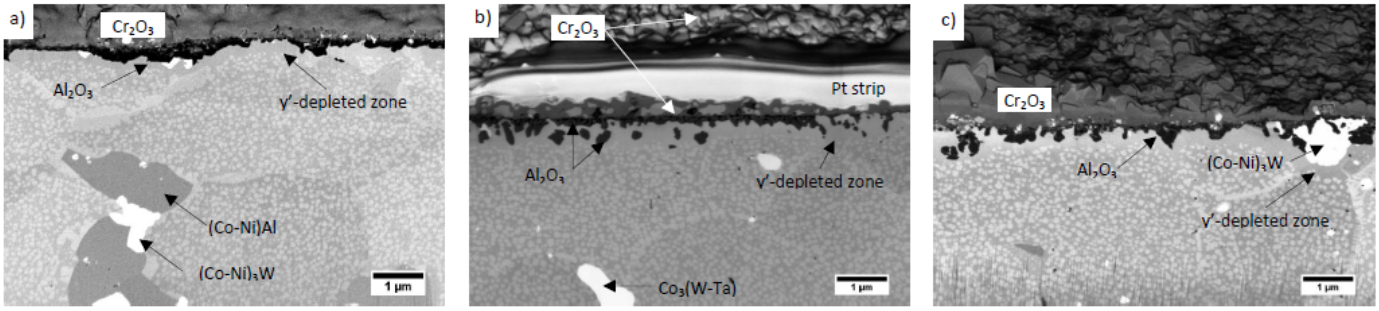

Figure 6: EsB-SEM micrographs of alloy (a) 17Cr-12Al (b) 15Cr-10Al (c) 1.3Co-17Cr-10Al microsctucture after oxidation at 800°C for 200 h showing FIB sections revealing the external and internal oxides, γ'-depleted zone, secondary phases in the bulk, and a fine γ/γ' microstructure in the base metal.

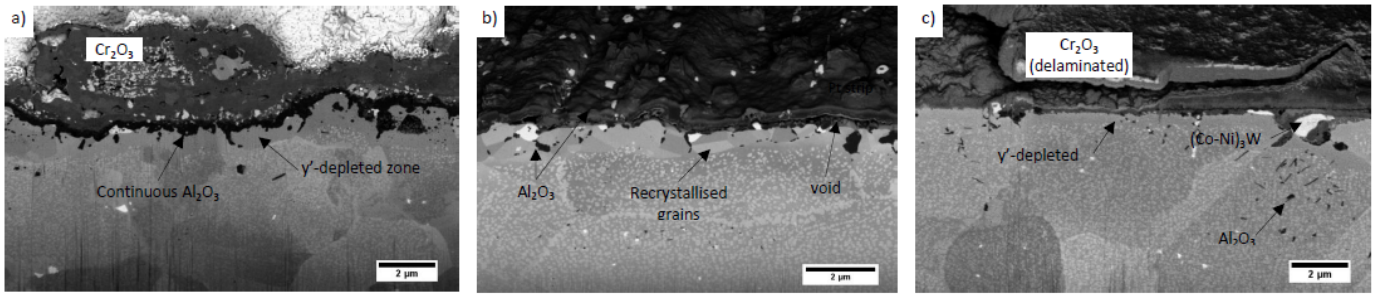

Figure 7: EsB-SEM micrographs of alloy (a) 17Cr-12Al (b) 15Cr-10Al (c) 1.3Co-17Cr-10Al microstructure after oxidation at 800°C for 300 h showing FIB sections revealing the external and internal oxides, γ'-depleted zone, secondary phases in the bulk, recrystallised grains at the γ'-depleted zone and a fine γ/γ' microstructure in the base metal.

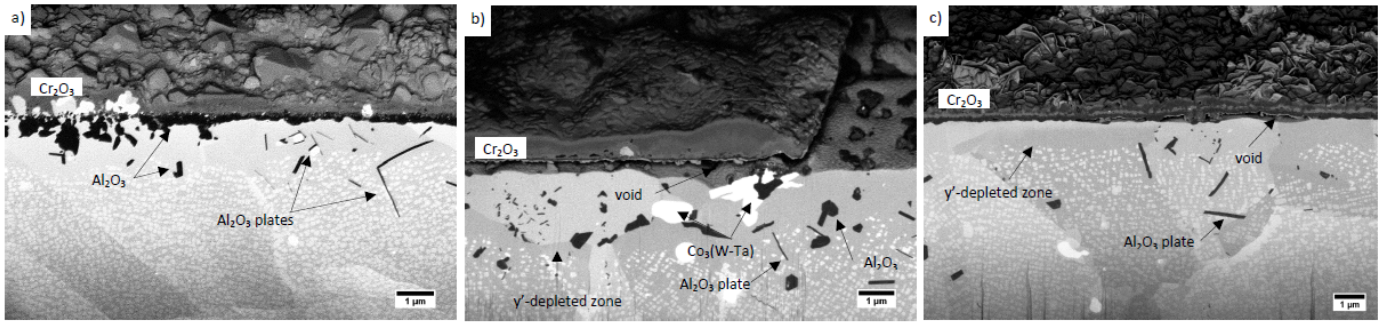

Figure 8: EsB-SEM microstructures of alloy 15Cr-10Al after oxidation at 800° for (a) 400 h (b) 1000 h (c) 2000 h showing FIB sections with external and internal oxides, voids, γ'-depleted zone, alumina plates, secondary phases in the bulk and a fine γ/γ' microstructure in the base metal.

spalled oxide in the crucible, delamination of external scale is an early sign of spallation. Also, there is an uncommon phase in the bulk as seen in Figure 7c with a plate-like morphology, which has the same contrast in EsB-SEM mode as the Al_2O_3 scale. Often in Ni superalloys, AlN can co-occur with alumina internal oxides, but in the present case no N signal was detected in STEM-EDX examination.

3.5. Long-term oxidation of alloy 15Cr-10Al

Since alloy 15Cr-10Al has less external oxide, a continuous internal Al_2O_3 layer, and no observed oxide delamination, it was selected for long-term oxidation trials at 400 h, 1000 h and 2000 h. After long-term oxidation at 800°C, severe internal oxidation took place in the oxide/alloy region as seen in Figure 8. STEM/EDX analysis was performed to determine the plate-like composition of the phase and it was found to be alumina, with no N found. After 1000 or more hours, the oxide scale delaminated, leaving the exposed surface unprotected. This caused rapid internal oxidation as observed in Figure 8.

3.6. FIB-SIMS elemental mapping

Figure 9 shows a FIB cross-section of the surface layers in alloy 15Cr-10Al following exposure at 800 °C for 200 h

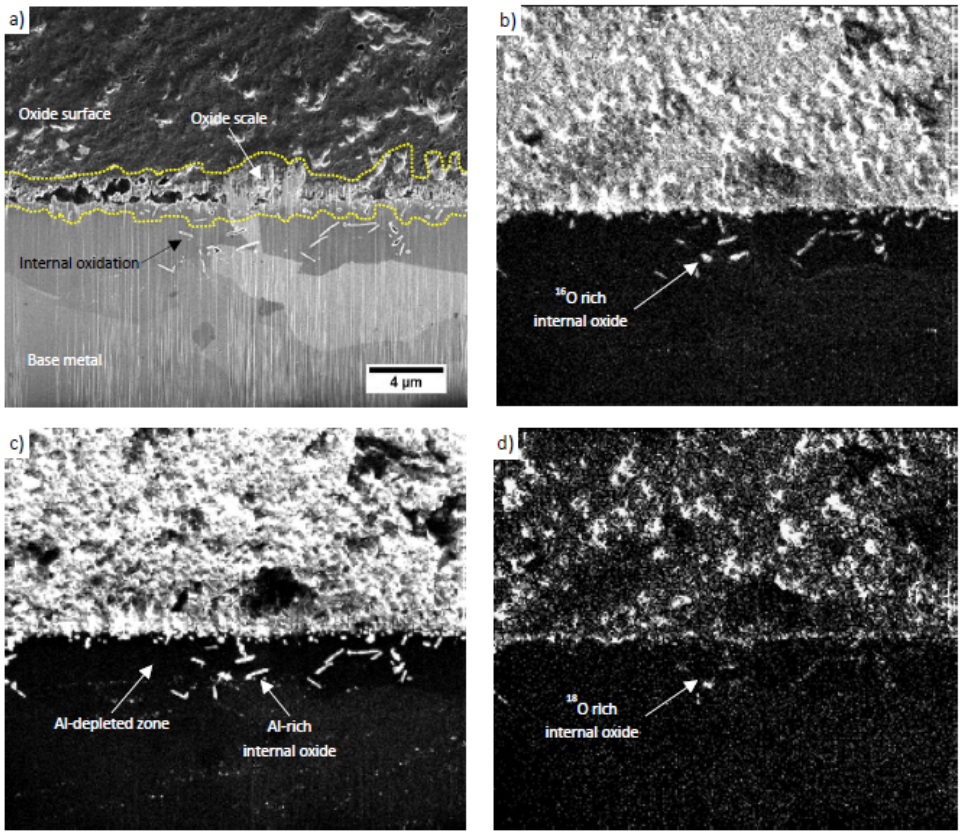

Figure 9: FIB oxide cross-section for alloy 15Cr-10Al following exposure in O_2 (200 mbar) at 800 °C for 200 h (a) FIB-SE image showing the oxide scale and internal oxide (b) FIB-SIMS elemental mapping of $^{16}O^-$ (c) FIB-SIMS elemental mapping of Al^+ (d) FIB-SIMS elemental mapping of $^{18}O^-$

(176 h in $^{16}O_2$ + 24 h in $^{18}O_2$). The FIB-SE image of the tapered oxide shows the surface of oxide, a section through the oxide scale containing alumina (dark contrast), the internal oxides, and the base metal. Figures 9 b - d show the FIB-SIMS $^{16}O^-$, $^{27}Al^+$ and $^{18}O^-$ elemental maps obtained using the cross sections in Figure 9 a. The FIB-SIMS maps of $^{16}O^-$ and $^{18}O^-$ show the relative distributions of the species. By normalising the pixel intensities to the maximum counts in each array, the $^{16}O^-$ map represents the oxide growth that occurs in the first part of the two-stage exposure. Note that the high intensity of $^{16}O^-$ signals in the outer oxide layer and some in the internal oxide correlate with the $^{27}Al^+$ signal. The $^{18}O^-$ ion distribution indicates that the oxide is enriched at the surface closest to gas/oxide region, oxide scale (alumina layer) and internal oxide region. This phenomena indicates that the new oxide is formed at the oxide/alloy region as well as gas/oxide interface. This finding is in line with the oxidation mechanism of Ni-based superalloy (RR1000) as reported by Foss et. al., where Cr_2O_3 typically grows through outward cationic diffusion which explains the new oxide at the gas/oxide region [26]. Therefore, it is reasonable to assume that the oxide grows through both inward diffusion of oxygen anions and outward diffusion of cations (chromium).

In order to eliminate any instrumental ionisation effect, the isotopic fraction was calculated from both FIB-SIMS maps of $^{16}O^-$ and $^{18}O^-$. The isotopic fraction f was calculated as the fraction of the detected oxygen signals I due to $^{18}O^-$,

$$f = \frac{I_{^{18}O^-}}{I_{^{16}O^-} + I_{^{18}O^-}} \quad (1)$$

Note that the isotopic fraction is normalised relative to the natural abundance (0.26%) and the tracer gas concentration (54%). It can be seen in Figure 10 that the $^{18}O^-$ enrichment is localised, at the oxide/alloy interface (alumina) and in the internal oxide (plate-like alumina) regions. The $^{16}O^-$ and $^{18}O^-$ intensity peaks in Figure 10 show high intensity in the oxide/alloy interface. The drop in $^{16}O^-$ intensity just before the oxide/alloy interface suggests oxygen diffusion through the external oxide scale.

3.7. STEM-EDX analysis

In order to better characterise the types of oxides that were formed, EDX mapping was performed on alloy 15Cr-10Al, oxidised for 200 h at 800°C. The STEM bright field (BF) image of alloy 15Cr-10Al in Figure 11 confirms the scales as seen in Figure 6b. The scale was comprised of

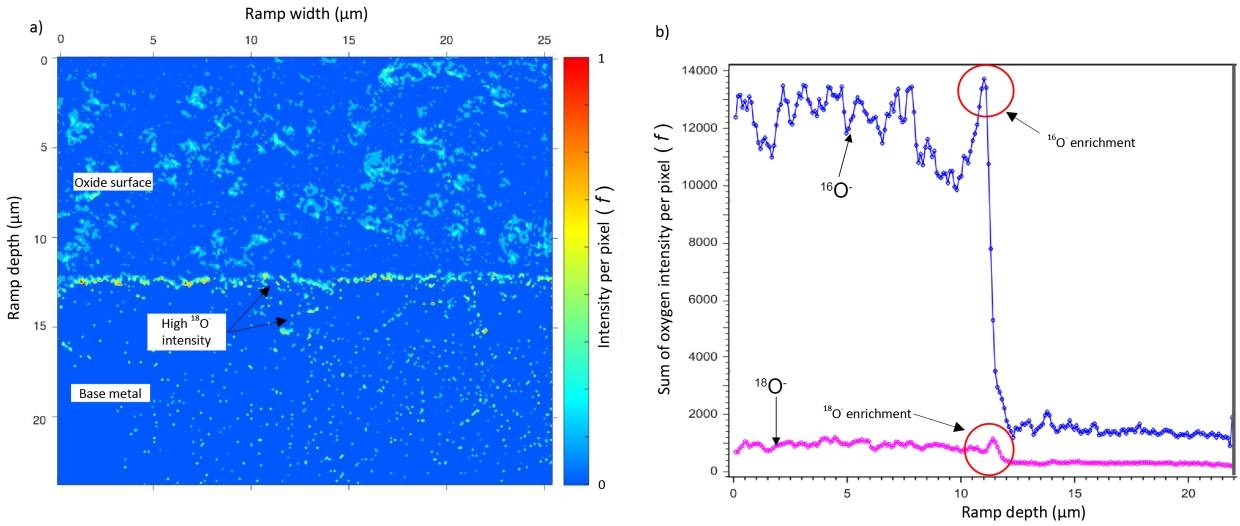

Figure 10: Isotopic enrichment of $^{18}O^-$ in alloy 15Cr-10Al oxidised at 800° for 200 h: (a) isotopic enrichment map and (b) $^{16}O^-$ and $^{18}O^-$ intensity peaks along the depth profile.

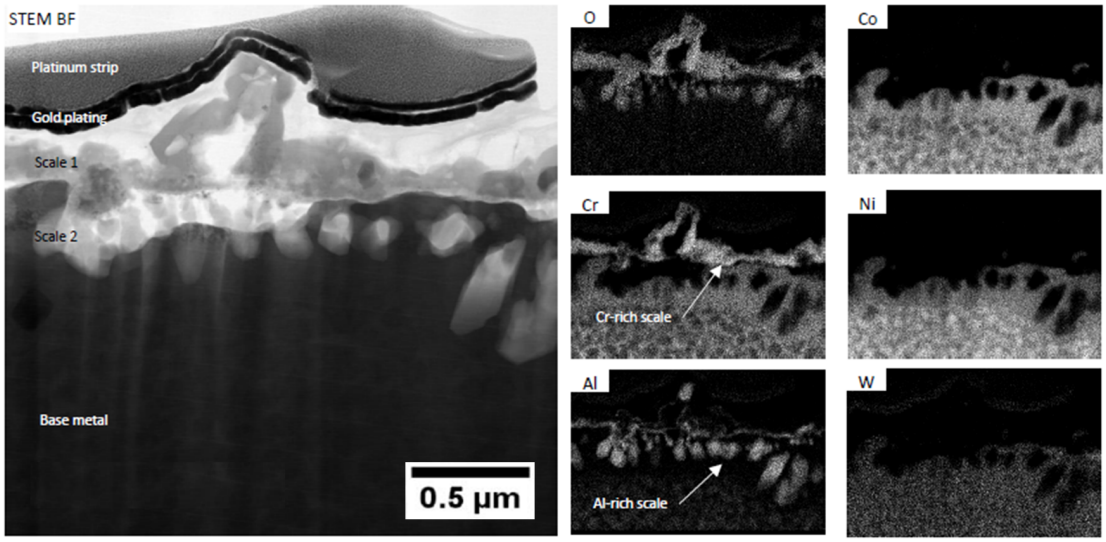

Figure 11: Bright field STEM image of alloy 15Cr-10Al oxidised for 200 h at 800°C showing a Cr-rich oxide scale (scale 1), an Al-rich internal oxide (scale 2). Cr and Co partition to the γ phase and Al, W and Ni to the γ'.

outer Cr-rich oxide (Scale 1) and inner Al-rich oxide. Due to the accuracy limitations of STEM-EDX analysis, the crystal structures of the oxides were determined using high resolution TEM (HRTEM) for stoichiometric determination.

A STEM dark field (DF) image of the same alloy was acquired in order to study the mechanism of oxidation during long-term exposure (300 h). Figure 12 is in agreement with the EsB-SEM result in Figure 7b, where delaminated external oxide and recrystallisation can be clearly observed in the γ'-depleted zone. Between the scale and the base metal, a cavity is present along the interface and the scale is supported by ligaments of Al-rich scale, which contained some chromia. It seems likely that surface scale is so thin that it cannot support a stress; therefore cavity formation occurs prior to spallation. In any case such cavity formation would seem to be deleterious to the oxidation performance of the alloy.

3.8. HRTEM

SEM-EDX and STEM-EDX results on alloy 15Cr-10Al, oxidised for 200 h at 800°C, provide initial indication of the compounds that form in this alloy series during oxidation. There were two distinct types of oxides; i) a Cr-rich external scale and ii) an Al-rich internal oxide. However, it is difficult to determine the crystal structures using selected area diffraction patterns as the oxides grains were too fine. Therefore, to identify the oxide compounds present in these layers, pseudo-diffraction patterns were obtained from individual grains in the TEM. The interplanar spacings were measured from Fourier transforms of

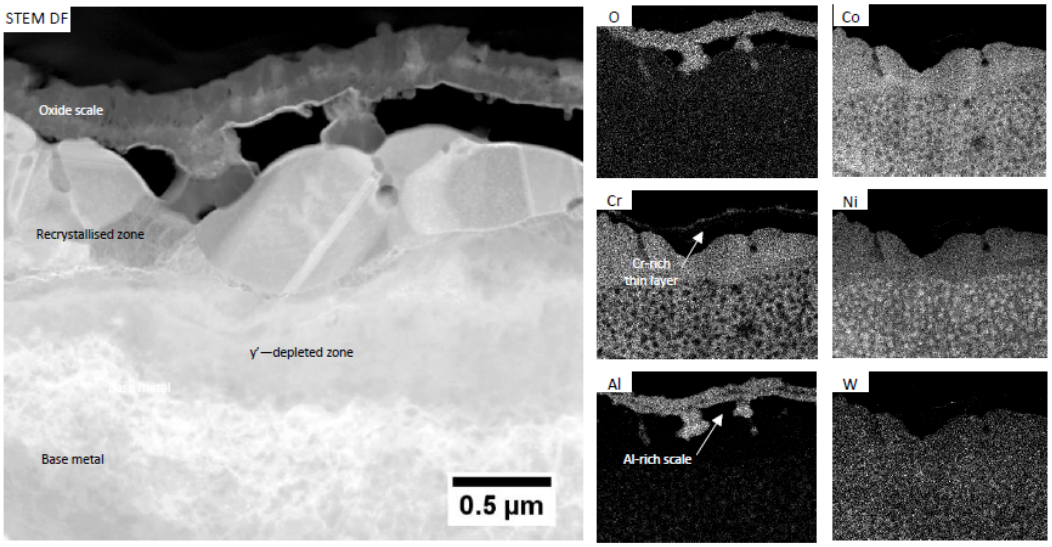

Figure 12: Dark field STEM image of alloy 15Cr-10Al oxidised for 300 h at 800°C showing a delaminated Al-rich oxide scale with a thin layer of chromia, Cr-Co-partition to γ and Al-W-Ni partition to the γ'.

the lattice images. The calculated lattice constants were compared to the literature values and thus the chemical identities of the oxides were determined. This approach is similar to the work of Yan et. al., where different layers of oxides with mixed spinels were successfully identified in a Co-7Al-7W-10Cr (at%) alloy [11].

The compositions of the two layers of oxides in alloy 15Cr-10Al were determined by point EDX and the averages were calculated. To confirm the oxide phase, high-resolution phase contrast lattice imaging were performed. The frequency domain images in Figure 13 were compared to simulated diffraction pattern generated using the Crystal Maker software.

By measuring the angles and distances between the spots in the frequency domain images and comparing them to the simulated diffraction patterns, the oxides labelled in Figure 14 are identified as A: Co_3O_4, B: Cr_2O_3, and C: Al_2O_3. The different oxide layers are also shown, in the same TEM foil, in Figure 11, which uses a different contrast optimisation. The average lattice constant of Co_3O_4 was measured to be 8.06 Å which is close to the lattice constant in the literature 8.17 Å [27]. Cr_2O_3 has a hexagonal structure with average measured lattice constants, a = 4.97 Å and c = 13.56 Å. The lattice constants in the literature are a = 4.96 Å and c = 13.59 Å [28]. The inner layer oxide is confirmed to be Al_2O_3 with an average calculated lattice constant of a = 4.29 Å and c = 12.24 Å. These measured lattice constants matched the trigonal structure found in the literature, with average lattice constants of a = 4.76 Å and c = 12.99 Å [29].

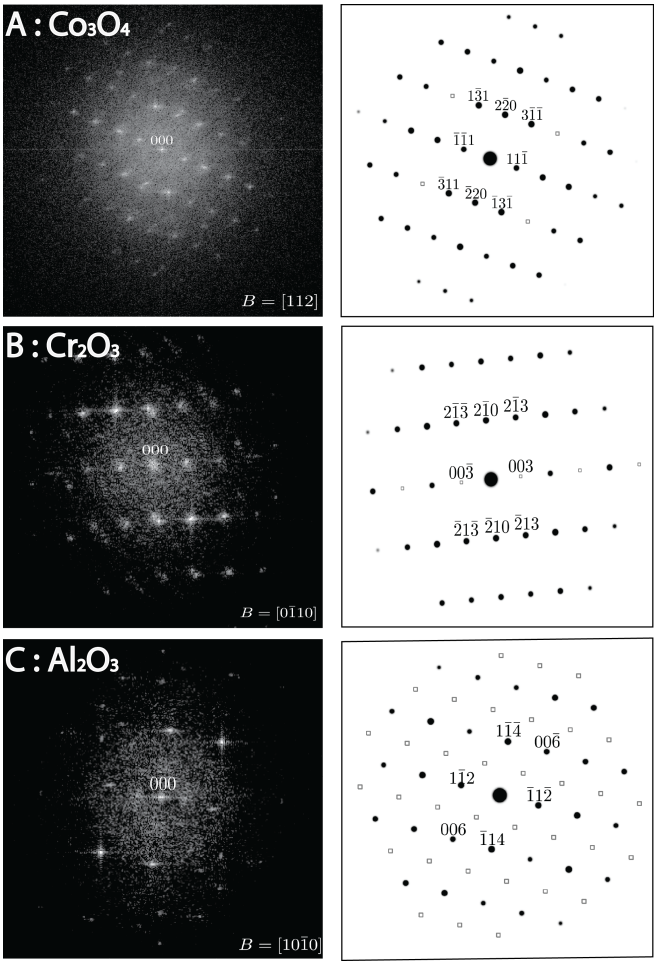

Figure 13: Frequency domain images (left) from the oxide scales in alloy 15Cr-10Al oxidised for 200 h at 800°C with a labelled zone axis and the corresponding simulated diffraction patterns (right). Systematic absences are represented by squares.

4. Discussion

The objective of this study has been the selection of the optimal Co:Ni ratio and the optimum fractions of Cr

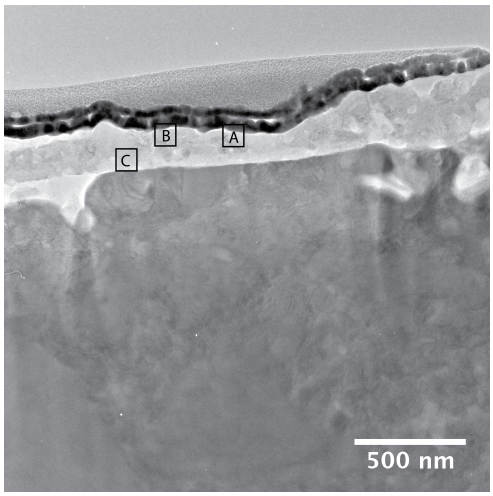

Figure 14: Overview of the oxidised alloy 15Cr-10Al after 200 h at 800°C obtained from a FIB-milled TEM foil using BF STEM imaging mode. Lattice images of grains in region A, B and C were obtained using HRTEM and frequency domain images were obtained using FFT in ImageJ.

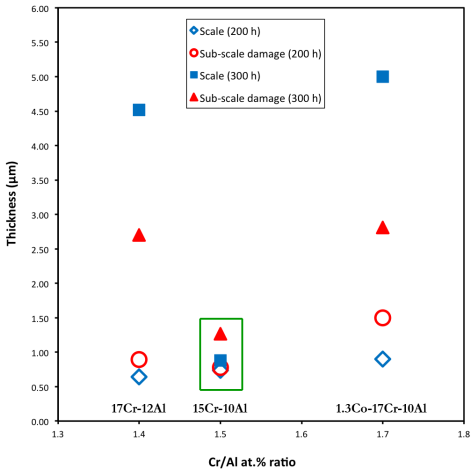

Figure 15: Variation of oxidation damage depth with Cr/Al atomic ratio.

and Al for obtaining the best oxidation resistance while maintaining a stable underlying microstructure. A typical cross-sectional microstructure of an oxidised sample can be divided into five zones: the external scale, the internal oxide, the γ'-depleted zone (containing ultra fine precipitates of γ' or sometimes recrystallised grains), the round edged γ' precipitates below that, and the typical cuboidal precipitates in the bulk alloy (as well as the secondary CoAl and Co_3W phases).

After 200 h of oxidation all three alloys exhibited a similar oxide morphology in which there were two external oxides (Cr and Al-rich scales) of sub-µm thickness and internal alumina grains, Figure 6. Distinctions between the three alloys could only be made after 300 h oxidation at 800°C, Figure 7. The differences noted were: (i) the external oxides were thickest in alloy 17Cr-12Al, (ii) that internal oxide intrusions formed in alloy 15Cr-10Al and (iii) that external oxide delamination was observed in alloy 1.3Co-17Cr-10Al.

Alloy 1.3Co-17Cr-10Al oxidised more rapidly compared to the other two alloys based on the thickness of the scales. Even with 10% Al, and higher Cr content (17%), the alloy exhibits poor oxidation resistance. The only possible reason for this is the amount of Co. As we change the Co:Ni ratio from 1:1 to 1.3:1, the oxidation resistance is reduced. Furthermore, as the Cr content was increased to 17%, the B2 secondary phase can be found in the bulk. It is crucial to understand the optimisation of Cr and Al content for the purpose of oxidation resistance while maintaining the desired mechanical properties by controlling the formation of secondary phases. Therefore, Figure 15 relates the optimum atomic ratio of Cr/Al to the oxidation damage depth after 200 h and 300 h of thermal exposure. The data suggest that the overall best Cr/Al atomic ratio is 1.5.

As the exposure time increased, the external oxide (Cr_2O_3) is not protective and the internal oxidation occurs to a greater depth, forming plate-like alumina in the bulk material. At the same time, alumina grows outward forming external scale that in some cases delaminates from the surface. The FIB-SIMS mapping reveals that there is $^{16}O^-$ and Al^- enrichment at the oxide/alloy interface (oxide intrusion) and that the new oxide ($^{18}O^-$-enrichment) is also formed in the vicinity of the metal-oxide interface. Nevertheless, it can be concluded from the maps that $^{16}O^-$ is observed in the inner part of the oxide scale, enriching the alumina scale and subsequently limiting further diffusion of $^{18}O^-$.

HRTEM results are in agreement with the established thermodynamic rules of partial pressure of oxygen [30], where at high oxygen partial pressure, the outer oxide layer is Co_3O_4, Cr_2O_3 underneath, and lastly Al_2O_3 forming the internal oxide at low oxygen partial pressure with low diffusivity of oxygen compared to the other two oxides.

5. Conclusions

In this study we have presented experimental evidence that oxidation-resistant, protective oxide scales can be formed in Co-Ni-Al-W-Cr superalloys. The following conclusions can be drawn:

1. 15 at.% of Cr and 10 at.% of Al produced a multilayer oxide scale and internal alumina which is protective and limits the inward diffusion of oxygen at 200 h, 800°C.
2. A very thin sub-µm oxide scale was formed in all the alloys after 200 h, 800°C oxidation. However, a high percentage of Cr and Co caused further oxidation of the samples at longer exposure times.
3. Significant internal oxidation was observed, with plate-like alumina forming during long-term oxidation, even with an optimum Cr/Al ratio.
4. Alloy 15Cr-10Al maintained a two phase γ/γ' microstructure with minimal secondary phase formation.

Acknowledgements

The authors would like to acknowledge the financial support provided by Rolls-Royce plc, Imperial College, EPSRC (grants EP/L001748/1, EP/M005607/1) and Majlis Amanah Rakyat (Government of Malaysia). We would also like to thank Dr. Richard J. Chater and Dr. Martin Weiser for their assistance.

References

[1] J. Sato, T. Omori, K. Oikawa, I. Ohnuma, R. Kainuma, and K. Ishida. Cobalt-base high-temperature alloys. *Science* 312 (2006) 90–91.

[2] M. Tsunekane, A. Suzuki, and T. M. Pollock. Single-crystal solidification of new Co-Al-W base alloys. *Intermetallics* 5 (2011) 636–643.

[3] A. Suzuki, J. Zhu, M. Tsukane, J. Dibbern, and T. M. Pollock. New Co-based γ/γ' high-temperature alloys. *JOM* 62 (2010) 58–63.

[4] H. Harada and H. Murakami. *Design of Ni-Base Superalloys*, pp. 39–70. Springer Berlin Heidelberg, Berlin, Heidelberg, 1999.

[5] Y. Yuan, Y.F. Gu, Z.H. Zhong, T. Osada, C.Y. Cui, T. Tetsui, T. Yokokawa, and H. Harada. Creep mechanisms of a new Ni-Co-base disc superalloy at an intermediate temperature. *J. Microsc.* 248 (2012) 34–41.

[6] A. Suzuki, A.J. Elliott, M.F.X. Gigliotti, K.B. Morey, J.C. Schaeffer, and P. Subramanian. Alumina-forming cobalt-nickel base alloy and method of making an article therefrom, May 19 2015. US Patent 9,034,247.

[7] A. Mottura, A. Janotti, and T.M. Pollock. Alloying effects in the γ/γ' phase of Co-based superalloys. In *Superalloys 2012*, pp. 683–693. Warrendale, PA: John Wiley & Sons Inc., 2012.

[8] A. Bauer, S Neumeier, F. Pyczak, and M. Goken. Creep strength and microstructure of polycrystalline γ/γ' strengthened Co-base superalloys. In *Superalloys 2012*, pp. 695–703. Warrendale, PA: John Wiley & Sons Inc., 2012.

[9] M. Ooshima, K. Tanaka, N. Okamoto, K. Kishida, and H. Inui. Effects of quaternary alloying elements on the γ'-solvus temperature of Co-Al-W based alloys with fcc/$L1_2$ two-phase microstructures. *J. Alloy. Compd.* 508 (2010) 71–78.

[10] L. Klein, M.S. Killian, and S. Virtanen. The effect of nickel and silicon addition on some oxidation properties of novel Co-based high temperature alloys. *Corros. Sci.* 69 (2013) 43–49.

[11] H.Y. Yan, V.A. Vorontsov, and D. Dye. Effect of alloying on the oxidation behaviour of Co-Al-W superalloys. *Corros. Sci.* 83 (2013) 382–395.

[12] M. P. Brady, I.G. Wright, and B. Gleeson. Alloy design strategies for promoting protective oxide-scale formation. *JOM* 52 (2000) 16–21.

[13] Y.T. Xu, T.D. Xia, J.Q. Yan, and W.J. Zhao. Effect of alloying elements on oxidation behavior of Co-Al-W alloys at high temperature. *The Chin. J. Non-Fer. Met.* 20 (2010) 2168–2177.

[14] L. Klein, Y. Shen, M.S. Killian, and S. Virtanen. Effect of B and Cr on the high temperature oxidation behaviour of novel γ/γ' strengthened Co-base superalloys. *Corros. Sci.* 53 (2011) 2713–2720.

[15] L. Klein, A. Bauer, S. Neumeier, M. Goken, and S. Virtanen. High temperature oxidation of γ'-strengthened Co-base superalloys. *Corros. Sci.* 53 (2011) 2027–2034.

[16] H.Y. Yan, V.A. Vorontsov, and D. Dye. Alloying effects in polycrystalline γ'-strengthened Co-Al-W base alloys. *Intermetallics* 48 (2014) 44–53.

[17] L. Klein and S. Virtanen. Corrosion properties of novel γ'-strengthened Co-base superalloys. *Corros. Sci.* 66 (2013) 233–241.

[18] F. Xue, M. Wang, and Q. Feng. Alloying effects on heat-treated microstructure in Co-Al-W-base superalloys at 1300°C and 900°C. In *Superalloys 2012*, pp. 813–821. Warrendale, PA: John Wiley & Sons, Inc., 2012.

[19] L. Klein and S. Virtanen. Electrochemical characterisation of novel γ/γ'-strengthened Co-base superalloys. *Electrochimica Acta* 76 (2012) 275–281.

[20] N. Vermaak, A. Mottura, and T. M. Pollock. Cyclic oxidation of high temperature coatings on new γ'-strengthened cobalt-based alloys. *Corros. Sci.* 75 (2013) 300–308.

[21] K. Shinagawa, T. Omori, J. Sato, K. Oikawa, I. Ohnuma, R. Kainuma, and K. Ishida. Phase equilibria and microstructure on γ/γ' phase in Co-Ni-Al-W system. *Mater. Trans.* 49 (2008) 1474–1479.

[22] H.Y. Yan, V.A. Vorontsov, J. Coakley, N.G. Jones, H.J. Stone, and D.Dye. Alloying and the micromechanics of Co-Al-W quaternary alloys. *Mat. Sci. Eng. A* 613 (2014) 201–208.

[23] F. S. Pettit and G.H. Meier. Oxidation and hot corrosion of superalloys. In *Superalloys 1984*, pp. 651–687. Warrendale, PA: John Wiley & Sons Inc., 1984.

[24] C. Wagner. Passivity and inhibition during the oxidation of metals at elevated temperatures. *Corros. Sci.* 5 (1965) 751–764.

[25] S. Kobayashi, Y. Tsukamoto, T. Takasugi, H. Chinen, T. Omori, K. Ishida, and S. Zaefferer. Determination of phase equilibria in the Co-rich Co-Al-W ternary system with a diffusion-couple technique. *Intermetallics* 17 (2009) 1085–1089.

[26] B.J. Foss, M.C. Hardy, D.J. Child, D.S. McPhail, and B.A. Shollock. Oxidation of a commercial Ni-based superalloy under static loading. *JOM* 66 (2014) 2516–2524.

[27] P.J. Brown and J.B. Forsyth. *The crystal structure of solids*. Structures and Properties of Solids, pp. 172. New York: Edward Arnold, 1973.

[28] R. Newnham and Y. Haan. Refinement of the α Al_2O_3, Ti_2O_3, V_2O_3 and Cr_2O_3 structures. *New Crystal Structures (Z. Kristallogr.)* 117 (1962) 235–237.

[29] L. Lutterotti and P. Scardi. Simultaneous structure and size-strain refinement by the Rietveld method. *J. Appl. Crystallogr.* 23 (1990) 246–252.

[30] H.J.T. Ellingham. Transactions and communications. *J. Soc. Chem. Ind.* 63 (1944) 125.